Materials Research. 2022; 25:e20210553
DOI: https://doi.org/10.1590/1980-5373-MR-2021-0553

Some Insight on the Heat-affected Zone Strengthening Mechanisms in Duplex Stainless Steels

***E.V. Morales*[a,b*], *G. Betancourt*[a], *L. Olaya*[b], *I.S. Bott*[b]**

[a]*Central University "Marta Abreu de Las Villas", Physics Department, Santa Clara, CP 54830, VC, Cuba.*
[b]*Pontifícia Universidade Católica do Rio de Janeiro (PUC-Rio), Departamento de Engenharia Química e de Materiais, Rua Marques de S. Vicente 225, Gavea, 22541900, Rio de Janeiro, RJ, Brasil.*

Received: October 22, 2021; Revised: January 20, 2022; Accepted: January 23, 2022

The paper shows that the strengthening mechanisms at the duplex stainless steels' heat-affected zone (HAZ) are sensitive to the volume fractions of the different austenite morphologies and the orientation relationships of these austenite morphologies with ferrite. Also, the nitrogen content in these phases and the ferrite grain size significantly influence the strengthening mechanisms at the HAZs for the tested cooling times. Considering their morphologies and geometrical distributions, the different austenite volume fractions were calculated for each cooling time at the HAZ corresponding to two duplex stainless steels (UNS S31803 and UNS S32304). Predictions of the main macroscopic mechanical properties, as the yield and ultimate tensile strengths, were developed by knowing the features of the local phases. This approach clarifies the contribution of the different strengthening mechanisms during the strain at the simulated HAZs of the studied duplex stainless steels.

Keywords: *Duplex stainless steel, yield strength, heat-affected zone, strengthening mechanisms, microhardness.*

1. Introduction

It is well known that duplex stainless steels (DSS) properties depend on the austenite-ferrite phase ratio, which is designed to be approximately 1:1. On the other hand, the mechanical properties of the DSS are commonly determined by the single-phase properties of ferrite δ and austenite γ and by the spatial distribution of constituents in the two-phase alloy. The single-phase properties depend on the chemical composition and microstructural parameters[1]. The spatial arrangement of the ferrite and austenite is markedly influenced by the technological processes carried out in these two-phase steels. The strengthening mechanisms and the mechanical properties of the single-phases are well different from the ones in the two-phase microstructures of the DSS[2,3]. Some works have proposed different stereological parameters to describe the microstructure's phase distribution to understand the stress-strain behavior in the DSSs[1,3,4]. However, this macroscopic stress-strain behavior is not possible without knowing the local phase features[3,5] which cannot be obtained from the tensile tests.

Most articles that have assessed the stress-strain behavior in these DSSs have applied some Hall-Petch-type relationship where the mechanical properties are dominated by the phase grain sizes and the ferrite fraction[6-10]. It is emphasized that in all these works, the ferrite matrix coexists with only one austenite morphology (duplex structures), where both grain sizes are well defined geometrically. A few studies have recently focused on the role of austenite in strengthening the DSSs[11,12]. According to the available literature, there are no reports concerning the influence of the different austenite morphologies on the stress-strain behavior at the heat-affected zones (heterogeneous structures) by welding processes or welding simulations in these DSSs.

The phase ratio γ/δ tends to deviate from 1:1 in the heat-affected zone (HAZ). This phase ratio is strongly dependent on the thermal weld cycle. High heat input will result in a good recovery of the phase ratio after high-temperature ferritization. In contrast, too low a heat input may lead to a limited austenite fraction with detrimental consequences for the properties[13]. At the same time, it must be borne in mind that an upper limit to heat input is set by the precipitation of intermetallic phases such as σ and χ, which will lead to a severe reduction in toughness[14,15]. On the contrary, the chromium nitrides (Cr2N and CrN) can precipitate at lower heat input depending on the alloy's cooling rate and nitrogen content[16-18].

This paper aims to assess the influence of the local phase features on the strengthening mechanisms that govern the stress-strain behavior (yield and ultimate tensile strengths) of the simulated HAZs corresponding to two commercial DSSs.

2. Experimental Procedure

Two commercial duplex stainless steels, the UNS S31803 available in the form of an extruded tube of 200 mm outer diameter and 8.15 mm wall thickness and the UNS S32304 in the form of a plate of 8.5 mm wall thickness, were used. The chemical compositions of these two alloys are listed in Table 1. Longitudinal and transversal samples to the rolling direction of the as-received steels were mechanically abraded using silicon carbide (SiC) papers followed by diamond paste (1 μm) polishing. After this, the polished samples were electrolytically etched in a 30% KOH solution at 6V for 20 s. The microstructures of the samples

*e-mail: valencia@uclv.edu.cu

Table 1. Chemical composition (wt.%) of the two DSSs (UNS S31803 and UNS S32304).

Elements	C	Cr	Ni	Mo	Mn	P	S	Si	Cu	N
UNS S31803	**0.026**	**22.6**	**5.23**	**3.2**	**0.85**	**0.025**	**0.004**	**0.49**	**0.13**	**0.12-0.13**
UNS S32304	**0.027**	**23.09**	**4.96**	**0.182**	**1.38**	**0.026**	**0.0042**	**0.338**	**0.433**	**0.11**

were examined by light optical microscopy and scanning electron microscopy (LOM and SEM).

A Gleeble 3800 thermo-mechanical simulator performed the HAZ simulations using cylindrical bars of 101.5 mm length and 6 mm diameter. These bars had a reduction (3 mm) of the diameter at the central part corresponding to the region where the HAZ was simulated. This reduction is made to guarantee that samples break in the HAZ region (very narrow) during the tensile test. Tensile tests were performed with an Instron 5985 universal testing machine at room temperature, where the strain rate was 3 mm/min. The above-reduced specimens had 10 mm gauge length and 3 mm diameter. The reduced cylindrical bars were sampled at the longitudinal section of the rolling direction. The applied thermal cycles are schematically shown in Figure 1. The programmed thermal cycles in the Gleeble simulator are in correspondence with the Rykalin-2D model.

A peak temperature of 1350 °C was reached at a rate of 350 ºC/s. A holding time of 2 s at this temperature followed by cooling at different rates up to 500 ºC to simulate different heat inputs and then water quenched. The typical temperature range accepted for the austenite reformation and precipitation of intermetallic compounds is between 1200-800 ºC[20] in these DSSs. The cooling time from 800 ºC to 500 ºC ($\Delta t_{8/5}$) is more accessible to measure accurately than that from 1200 ºC to 800 ºC ($\Delta t_{12/8}$). In the following, we refer to $\Delta t_{12/8}$, which can be calculated by measuring the $\Delta t_{8/5}$ according to

$$\frac{\Delta t 8/5}{\Delta t 12/8} = \frac{\frac{1}{(500-T_0)^2} - \frac{1}{(800-T_0)^2}}{\frac{1}{(800-T_0)^2} - \frac{1}{(1200-T_0)^2}}$$ [20].

The microstructures of the normal surfaces to the long sample direction of the simulated HAZs, before tensile tests, were examined using LOM (ZEISS *Axioplan2 Imaging*) and transmission electron microscopy (TEM-Jeol 2010 operated at 200 kV). The (δ/γ) phase ratios and the austenite morphological forms in the HAZ microstructures were obtained by processing a representative number of light optical images using the AxioVision 4.8.2 and Fiji software.

Thin-foil samples for TEM were prepared by cutting a 200 mm-thick slice from the sectioned HAZ samples, punching 3-mm diameter disks from the slice, and electropolishing the disks in a Tenupol-5 apparatus using a solution of 10% perchloric acid and 90% ethylic alcohol at 0 ºC and 20 V.

Vickers microhardness measurements were carried out on the different austenite morphological forms and ferrite grains in the cross-sections of specimens. The specimen surfaces were carefully polished before indenting. Loads of 0.025 Kg ($HV_{0.025}$) and 0.050Kg ($HV_{0.05}$) were applied during 10 s.

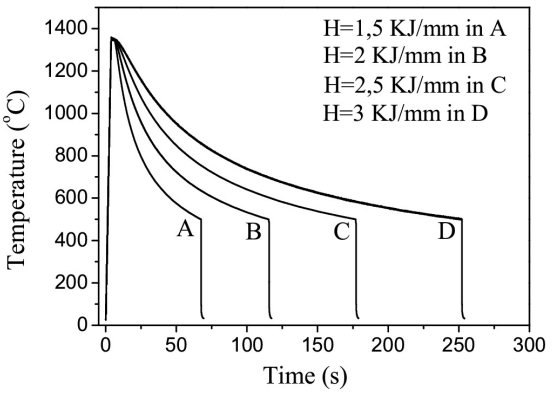

Figure 1. The Gleeble simulated thermal cycles corresponding to different heat inputs (H). The heating rate was 350 ºC/s and the corresponding cooling rates between 1350 ºC and 500 ºC were 13.8 ºC/s(A), 7.8 ºC/s(B), 5 ºC/s(C) and 3.5 ºC/s(D) respectively. (Morales et al.[19]).

3. Results

3.1. Microstructure of the HAZ

A statistical analysis of 30 processed optical micrographs of the HAZ microstructures before tensile tests allowed the quantification of the different austenite morphologies for each cooling time in the two DSSs. Three austenite morphological forms were identified at the HAZ microstructures, the grain boundary austenite (GBA), the intragranular austenite (IGA), and the Widmanstätten austenite (WA). The reformed austenite fractions with different morphologies are evaluated for each ferrite grain in the light optical micrographs. Each micrograph collected the information of approximately 5-10 ferritic grains depending on the cooling rate. This provided information of about 200 ferritic grains oriented randomly. Thus, the uncertainty by considering as IGA particles the WA laths (or needles) that have been cut normal to its growth direction on the micrograph plane was reduced. Also, a determined aspect ratio among the austenite particles within the ferrite grains was considered. Besides, the fragments from the WA laths formed at lower temperatures were also considered IGA precipitates. Intermetallic phases like σ and χ were not detected in the HAZ microstructures in these DSSs by LOM and SEM for the tested cooling times.

Figure 2ab shows the original and processed light optical images of the different morphological forms of austenite at different cooling times at the HAZ microstructures of both duplex stainless steels. In these figures, the WA laths are almost identically oriented in each ferrite grain, growing from a particular austenite grain boundary with approximately the same shape or within the grain itself. It is emphasized that the amount of IGA is concentrated and abounds in grains

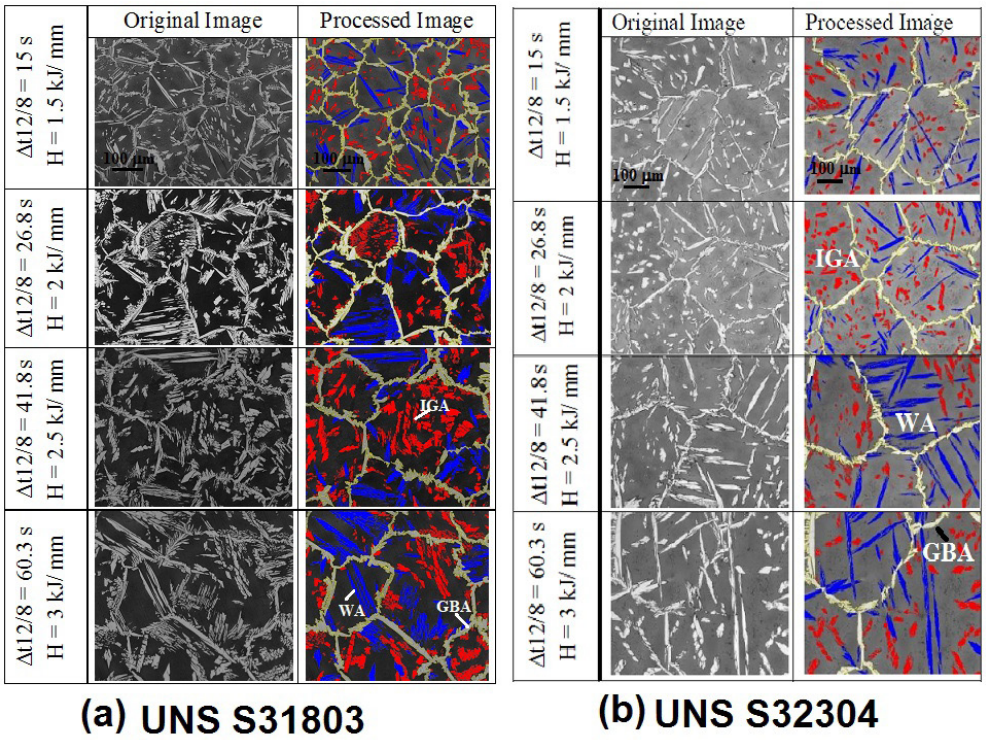

Figure 2. (a) Original and digital processed optical images of the simulated HAZs at different cooling times corresponding to the UNS S31803 DSS. (Morales et al.[19]); **(b)**: Original and digital processed optical images of the simulated HAZs at different cooling times corresponding to the UNS S32304 DSS. (*In these digital processed images, the IGA particles are in red color, the WA laths are in blue color and the grain boundary austenite (GBA) is in white-grey color*).

where the WA has not a strong presence. This indicates that the IGA is formed at lower temperatures after the WA nucleation. Figure 3 shows the austenite and ferrite volume fractions of the simulated HAZ microstructures for each cooling time (heat input) in both DSSs. The volume fractions of the phases taking into account their morphologies and the main microstructural parameters of the simulated HAZs at different cooling times, are given in Tables 2, 3, 4 and 5 for the two DSSs.

The austenite fraction in the HAZ microstructures of the UNS S31803 DSS is greater than the austenite fraction in the corresponding HAZ microstructures of the UNS S32304 DSS for the exact cooling times. Also, the increase (increasing rate) of the austenite fraction at the HAZ microstructures is smaller for larger cooling times in both DSSs. The GBA volume fraction is predominant for all studied cooling times in all the HAZ microstructures. Still, this predominance is more significant for the HAZ microstructures corresponding to the UNS S31803 DSS.

Tables 3 and 5 show that the ferrite grain size of the HAZ microstructures of the UNS S32304 DSS is approximate twice the ferrite grain size corresponding to the HAZ microstructures of the UNS S31803 DSS for the same cooling times. The GBA average width increases significantly at shorter cooling times at the HAZ microstructures of the two DSSs. The average length of the WA laths increases in correspondence with the average ferrite grain size at the simulated HAZs of both DSSs. The average size of the IGA

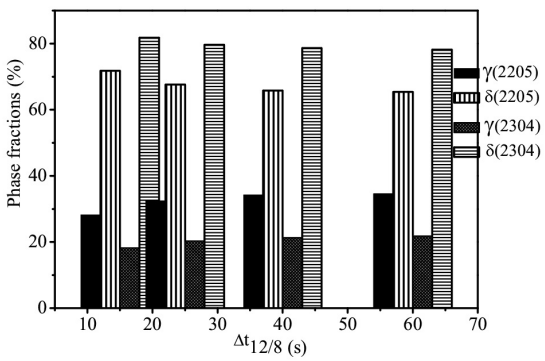

Figure 3. Austenite and ferrite volume fractions at the HAZs of the UNS S31803 and UNS S32304 DSSs for different cooling times.

precipitates and the average width of the WA laths does not show significant changes at the HAZ microstructures in these DSSs for the tested cooling times.

Many small IGA precipitates (or fragmented WA laths) within ten random ferrite grains corresponding to the HAZs for the shorter cooling time in both DSS were carefully observed by TEM. The boundaries with specific orientation relationships (ORs) between the small austenite particles and ferrite turned out to predominate in the observed HAZ microstructures. Figure 4ab shows the bright-field images corresponding to two representative IGA particles

Table 2. Austenite (V_γ) and ferrite (V_δ) volume fractions at different cooling times at the HAZ microstructures of the UNS S31803 DSS. . V_{GBA}, V_{IGA} and V_{WA} are the austenite volume fractions taking into account their morphologies. Heat input (H), the ξ_{IGA}, ξ_{GBA}, and ξ_{WA} are the ratios between the volume fraction of the different austenite morphologies and the total austenite volume fraction.

$H_{(KJ/mm)}$	$\Delta t_{8/5(s)}$	$\Delta t_{12/8(s)}$	$V_{\gamma(\%)}$	$V_{\delta(\%)}$	$V_{IGA(\%)}$	$V_{GBA(\%)}$	$V_{WA(\%)}$	ξ_{IGA}	ξ_{GBA}	ξ_{WA}
1.5	43	15	28.2	71.8	8.9	14.0	5.3	31.4	49.7	19.0
2	76	25	32.4	67.6	9.0	15.8	7.6	27.7	48.8	23.5
2.5	118	40	34.2	65.8	10.0	16.0	8.2	29.3	46.7	23.9
3	170	60	34.6	65.4	11.9	13.6	9.0	34.7	39.1	26.2

Table 3. Microstructural parameters of the simulated HAZs corresponding to the UNS S31803 DSS at different cooling times. Average grain size of ferrite (d), average width of the GBA (A_{GBA}), average length of the WA laths (l_{WA}), average radius of the IGA particles (R_{IGA}) and average width of the WA laths (A_{WA}).

H (KJ/mm)	$\Delta t_{8/5}$ (s)	$\Delta t_{12/8}$ (s)	d (μm)	$A_{GBA(\mu m)}$	$l_{WA(\mu m)}$	$R_{IGA(\mu m)}$	$A_{WA(\mu m)}$
1.5	43	15	104.6	8.9	28.5	2.1	3.1
2	76	25	136.3	13.2	32.2	2.6	4.2
2.5	118	40	160.8	14.4	33.3	2.8	4.2
3	170	60	184.5	14.1	36.4	3.1	4.3

Table 4: Austenite (V_γ) and ferrite (V_δ) volume fractions at different cooling times at the HAZ microstructures of the UNS S32304 **DSS.** V_{GBA}, V_{IGA} and V_{WA} are the austenite volume fractions taking into account their morphologies. Heat input (H), the ξ_{IGA}, ξ_{GBA}, and ξ_{WA} are the ratios between the volume fraction of the different austenite morphologies and the total austenite volume fraction.

$H_{(KJ/mm)}$	$\Delta t_{8/5(s)}$	$\Delta t_{12/8(s)}$	$V_{\gamma(\%)}$	$V_{\delta(\%)}$	$V_{IGA(\%)}$	$V_{GBA(\%)}$	$V_{WA(\%)}$	ξ_{IGA}	ξ_{GBA}	ξ_{WA}
1.5	43	15	18.2	81.8	5.3	6.6	5.6	29.1	36.3	30.8
2	76	25	20.3	79.7	6.1	9.4	5.9	30.0	46.3	29.1
2.5	118	40	21.3	78.7	6.8	7.6	6.9	31.9	35.7	32.4
3	170	60	21.8	78.2	7.2	7.5	7.2	33.0	34.4	33.0

Table 5. Microstructural parameters of the simulated HAZs corresponding to the UNS S32304 DSS at different cooling times. Average grain size of ferrite (d), average width of the GBA (A_{GBA}), average length of the WA laths (l_{WA}), average radius of the IGA particles (R_{IGA}) and average width of the WA laths (A_{WA}).

H (KJ/mm)	$\Delta t_{8/5}$ (s)	$\Delta t_{12/8}$ (s)	d (μm)	$A_{GBA(\mu m)}$	$l_{WA(\mu m)}$	$R_{IGA(\mu m)}$	$A_{WA(\mu m)}$
1.5	43	15	193.2	7.8	39,9	2.3	4.2
2	76	25	229.5	10.1	44.1	2.4	4.3
2.5	118	40	240.1	11.3	44.6	2.6	4.5
3	170	60	297.1	12	45.4	2.9	4.9

corresponding to the HAZ microstructures of both DSS with a shorter cooling time. Structural dislocations, periodically spaced, can be observed in the broad faces of the IGA particles. These small precipitates seem to have nucleated from the forest of dislocations in the matrix.

3.2. The hardness and tensile properties of the HAZ

Figure 5 shows the microhardness measurements of the different austenite morphologies and the ferrite matrix before tensile tests, corresponding to the simulated HAZ microstructures of the two DSSs. The average hardness values in each austenite morphology and ferrite did not have appreciable differences by using loads of 25 and 50 g, respectively. Most indentations with both loads showed a typical "pile-up" morphology (the shape of indentation is square with straight edges where the plastic deformation is concentrated in a relatively small area near the indentation)[21]. For such reason, a load of 25 g was used, taking into account the small size of the different austenite morphologies to avoid the grain boundary effects on the hardness values. The hardness of the WA laths and IGA precipitates is significantly higher than the GBA hardness in all HAZ microstructures of both DSSs.

The austenite hardness values independent of their morphologies are always higher than the hardness values measured in ferrite at the different cooling times in these HAZs of the two DSSs. Figure 6 shows the normalized hardness, $(\hat{H}-H_s)/(H_h-H_s)$, of the HAZ microstructures in both

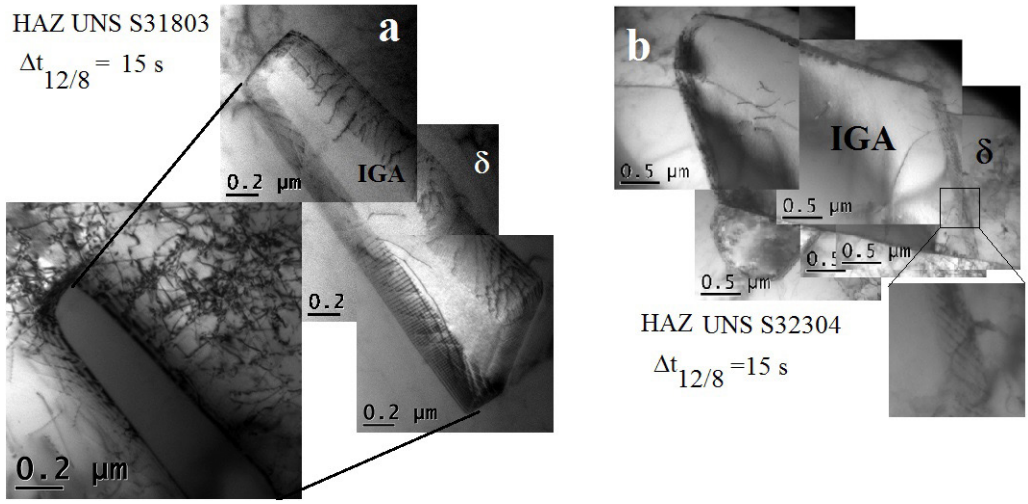

Figure 4. TEM bright field images of two representative IGA particles corresponding to the HAZs with the shorter cooling time of both DSS. The misfit dislocations can be observed at the broad faces. (Figure 4a in Morales et al.[19]).

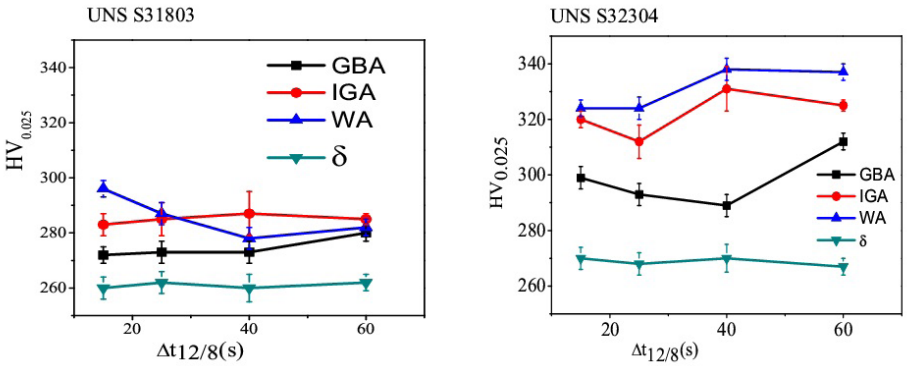

Figure 5. The hardness values of the different austenite morphological forms and ferrite corresponding to the HAZ microstructures at the tested cooling times of the UNS S31803 and UNS S32304 DSSs.

DSSs for all cooling times, where $\hat{H}=\sum_i \overline{HV}_i^{\gamma} V_i^{\gamma} + \overline{HV}^{\delta} V^{\delta}$ (i=GBA, IGA, WA), H_s is the average hardness of the soft phase (ferrite) and H_h is the average hardness of the hard phase (WA or IGA).

Three HAZ samples with the same cooling time were tested to obtain the average yield (0.2% plastic strain, $\sigma_{y0.2}$) and ultimate tensile strengths in the tensile tests at room temperature. The engineering stress-strain curves obtained of the tensile tests showed that the yield (0.2% plastic strain) and ultimate tensile strengths are not significantly different. The ratios between ultimate tensile strength and the yield strength, Figure 7, ($\sigma_{UTS}/\sigma_{y0.2}$) are between 1.07 and 1.04 for all the simulated HAZ samples at different cooling times in both DSSs. Figure 8 shows the average engineering yield ($\sigma_{y0.2}$) and ultimate tensile (σ_{UTS}) strengths of the simulated HAZs at different cooling times in both DSSs. The tensile properties at the simulated HAZ samples of the UNS S31803 DSS are higher than the one at the simulated HAZ samples corresponding to the UNS S32304 DSS.

4. Prediction of the Mechanical Properties at the Simulated HAZ

In this section, various strengthening models used to forecast the yield strength will be reviewed and compared to experimental results corresponding to the DSS HAZs. Assessing the interrelation between microstructure and strength in two-phase structures, as in the DSS, is more complex than in the single phases. Ferrite is usually stronger than austenite for the same interstitial content. The solubility of carbon and nitrogen in austenite is much higher than in the ferrite matrix. Therefore, in duplex structures, the nitrogen is partitioned so that austenite can become stronger than ferrite[2,22]. To establish a relationship between the microstructure of the annealed duplex steels and the yield strength, some researchers have used the well-known mixture law[7,9]. This mixture rule in the simplest form establishes that the yield stress of the compound (σ_y) is given by a simple superposition of the average yield stresses (σ_y^i) of the constituents multiplied by their respective volumetric amounts (V^i) in the sample. In duplex steels (γ and δ phases), this relationship could serve as a crude estimate of the yield strength:

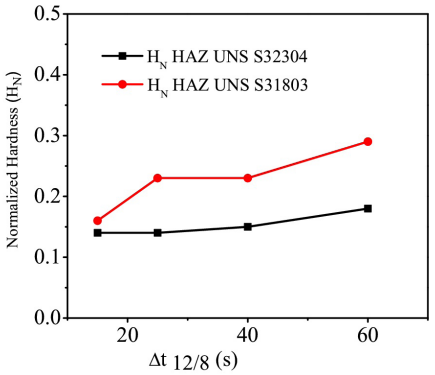

Figure 6. Normalized hardness of the HAZs at different cooling times for both DSSs (UNS S31803 and UNS S32304).

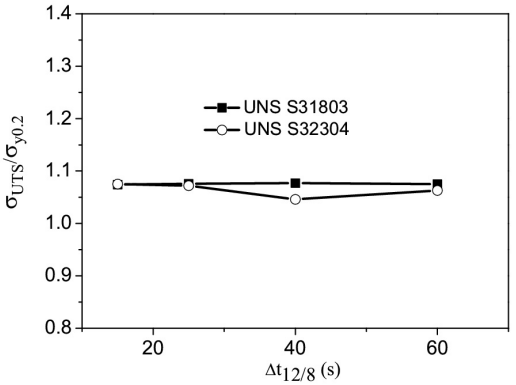

Figure 7. The ultimate tensile strength (σ_{UTS}) and yield strength ($\sigma_{y0.2}$) ratios at different cooling times corresponding to the HAZs of the UNS S31803 and UNS S 32304 DSSs.

$$\sigma_y = \sigma_y^{\gamma} V^{\gamma} + \sigma_y^{\delta} V^{\delta} \quad (1)$$

A more general empirical law of mixtures was suggested by Tamura et al.[23], where the yield stress of each phase is replaced by their average values respectively:

$$\sigma_y = \overline{\sigma}_y^{\gamma} V^{\gamma} + \overline{\sigma}_y^{\delta} V^{\delta} \quad (2)$$

This new relationship was called the modified law of mixtures, where the interaction effects are incorporated into the stress values associated with each phase.

Furthermore, it is common to calculate the yield stress of the individual phases in the DSSs to use the well-known relationship between the hardness (HV) and the yield strength as $HV \cong 3\sigma_y$[24-27]. Thus, the average yield stresses of the constituents are calculated by their average hardness values. Then, extending the modified mixture law, Equation 2, to all constituents (different austenite morphologies and ferrite) at the HAZ microstructures in these DSSs, the following correlation can be obtained:

$$\sigma_{yI} = \sum_i \left(\frac{\overline{HV}}{3}\right)_i^{\gamma} V_i^{\gamma} + \left(\frac{\overline{HV}}{3}\right)^{\delta} V^{\delta}, \quad (3)$$

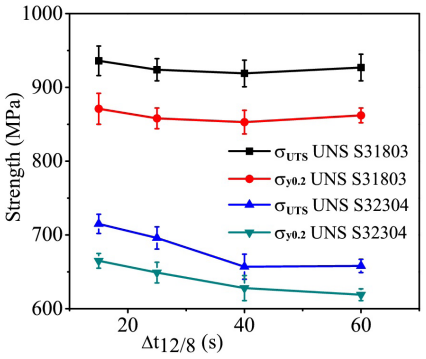

Figure 8. The experimental ultimate tensile strength (σ_{UTS}) and yield strength ($\sigma_{y0.2}$) values corresponding to the simulated HAZs at different cooling times of the UNS S31803 and UNS S32304 DSSs.

where V_i^{γ} is the volume fraction of the different austenite morphologies (i=GBA, IGA, WA). This equation does not include the explicit dependence on grain size[1,21]. Also, in annealed DSS structures[1], the austenite and ferrite yield stresses (σ_y^{γ}, σ_y^{δ}) are calculated, considering the character of the interfaces. Thus, for the ferrite phase was obtained the following expression[1]:

$$\sigma_y^{\delta} = \sigma_y^{\delta b} + \Delta\sigma_y^{\delta(SS+P)}\left(C_N^{\delta}\right) + \frac{K^{\delta b}}{\sqrt{L_{\delta}}}, \quad (4)$$

with $\sigma_y^{\delta b} = 440\,MPa$ (the friction stress of the nitrogen-free ferritic base material)[1], $\Delta\sigma_y^{\delta(SS+P)}\left(C_N^{\delta}\right) = 156\,C_N^{\delta}$ MPa/wt% (the flow stress caused by solid solution and particle strengthening)[1,28], $C_N^{\delta} = 0.1\%$[29] (maximum nitrogen content in the alloyed ferrite), $K^{\delta b} = 20$ Nmm$^{-3/2}$ (the grain size coefficient of the ferritic base material)[30] and $\overline{L_{\delta}}$ the average ferrite grain size in the duplex structure[1].

Representative grain size of the different austenite morphologies at the HAZ microstructure is challenging to estimate the austenite yield stress according to Horvath et al.[1]. Therefore, the yield stress for each austenite morphological form is calculated by the well-accepted relationship between hardness and yield strength, $HV \cong 3\sigma_y$. The ferrite yield stress is calculated according to Equation 4, where $\overline{L_{\delta}}$' is now the ferrite average grain size corresponding to each HAZ microstructure. Thus, a mixture rule that incorporates the Hall-Petch-type Equation 4 for the ferrite matrix in these heterogeneous structures can be written as

$$\sigma_{yII} = \sum_i \left(\frac{\overline{HV}}{3}\right)_i^{\gamma} V_i^{\gamma} + \left(\sigma_y^{\delta b} + \Delta\sigma_y^{\delta(SS+P)}\left(C_N^{\delta}\right) + \frac{K^{\delta b}}{\sqrt{L_{\delta'}}}\right) V^{\delta}, \quad (5)$$

As the microhardness ratio of the constituent phases can be used as an approximate measure for the yield strength ratio of these phases at the HAZ microstructures[31,32], a similar relationship also can be obtained:

$$\sigma_{yIII}=\left\{\left[\frac{(\overline{HV})^{\gamma}}{(\overline{HV})^{\delta}}\right]V^{\gamma}+V^{\delta}\right\}\left(\sigma_y^{\delta b}+\Delta\sigma_y^{\delta(SS+P)}\left(C_N^{\delta}\right)+\frac{K^{\delta b}}{\sqrt{L_{\delta'}}}\right), \quad (6)$$

where $\left(\overline{HV}\right)^{\gamma}=\frac{1}{3}\sum_i(\overline{HV})_i^{\gamma}$ (i=GBA, IGA, WA) and V^{γ} is the total austenite volume fraction.

A fourth approach, can be employed considering separately the yield stress of each austenite morphological form expressed in the mixture rule (Equation 6) as average microhardness ratios between each austenite morphological form and ferrite:

$$\sigma_{yIV}=\{(\sum_i\left[\frac{(\overline{HV})_i^{\gamma}}{(\overline{HV})^{\delta}}\right]V_i^{\gamma})+V^{\delta}\}\left(\sigma_y^{\delta b}+\Delta\sigma_y^{\delta(SS+P)}\left(C_N^{\delta}\right)+\frac{K^{\delta b}}{\sqrt{L_{\delta'}}}\right), \quad (7)$$

i=GBA, IGA and WA.

On the other hand, a combination of the relationships published by Nam et al.[33] and Hirota et al.[6] could be employed to estimate the yield stress of the different austenite morphologies at the HAZ in these DSSs. In Hirota et al.[6], the Hall-Pecth coefficient, k_y^{γ}, for a single γ-phase in SUS316L was 164 MPaμm$^{-0.5}$, and the average friction stress σ_0^{γ} resulted in 211 MPa. Then, the yield stress of austenite in SUS316L[6] was estimated as:

$$\sigma_y^{\gamma}=211+164D_{\gamma}^{-1/2}. \quad (8)$$

According to Nam et al.[33] and Hirota et al.[6], a compound mixture law can be suitable to determine the yield strength at the simulated HAZs of the DSSs as:

$$\sigma_y=\sum_i\left(211+164R_{\gamma i}^{-\frac{1}{2}}\right)V_i^{\gamma}+\sigma_y^{\delta}V^{\delta}, \quad (9)$$

where the $R_{\gamma i}$ are the average widths of the GBA and WA laths, and the average diameter of the IGA particles, (i=GBA, WA, IGA).

Sieurin et al.[34] reported that the hardening coefficient of each element (in wt. %) has a strong effect on *k*. The coefficients for each component are deduced from the linear regression of the yield strength equation 7Cr+20Mn+33Si+2.9Ni+77(N)[1/2 33]. Hence, k_y^{γ} resulted in approximately 191 MPa for the UNS S31803 and 198 MPa for the UNS S32304. To do this, it was assumed that the different austenite morphologies have roughly the same chemical composition given by the little mobility of the substitutional elements at the tested cooling times in the simulated HAZs. As σ_y^{δ} is expressed by a Hall-Petch-type Equation 4, a compound mixture law could be employed to estimate the yield strength at the HAZs of these two DSSs as:

$$\sigma_{yV}=\sum_i\left(211+191R_{\gamma i}^{-\frac{1}{2}}\right)V_i^{\gamma}+\left(\sigma_y^{\delta b}+\Delta\sigma_y^{\delta(SS+P)}\left(C_N^{\delta}\right)+\frac{K^{\delta b}}{\sqrt{L_{\delta'}}}\right)V^{\delta}, \quad (10)$$

for the UNS S31803

and,

$$\sigma_{yV}=\sum_i\left(211+198R_{\gamma i}^{-\frac{1}{2}}\right)V_i^{\gamma}+\left(\sigma_y^{\delta b}+\Delta\sigma_y^{\delta(SS+P)}\left(C_N^{\delta}\right)+\frac{K^{\delta b}}{\sqrt{L_{\delta'}}}\right)V^{\delta}, \quad (11)$$

for the UNS S32304

Tables 6 and 7 show the application of the different empirical approaches to estimate the yield strength at the simulated HAZs in these duplex stainless steels with varying cooling times. The values shown in the above tables have been depicted in Figure 9 for a better appreciation of the correspondence of the different approaches with the experimental tensile test results.

5. Discussion

5.1. Microstructural analysis

The austenite volume fraction increases with the cooling time at the simulated HAZs of both DSSs. This increase of the austenite fraction with the cooling time or heat input is in agreement with the literature[33-38], Tables 2 and 4. However, a decrease in the increasing rate of the austenite volume fraction can be appreciated for the longer cooling times.

Table 6. Experimental yield ($\sigma_{y0.2}$) and ultimate tensile strengths (σ_{UTS}). Yield strength values calculated through the different approaches $\sigma_{yI\text{-}V}$ corresponding to the HAZ microstructures at the tested cooling times in the UNS S31803 DSS. The $\sigma_{y0.2}$ and σ_{UTS} values of the as-receive samples were 837 MPa and 961 MPa respectively.

$\Delta t_{12/8}$, s	$\frac{\sigma_{y0.2}\pm\delta\sigma_{y0.2}}{\sigma_{UTS}\pm\delta\sigma_{UTS}}$ (exp.) (MPa)	σ_{yI} (MPa)	σ_{yII} (MPa)	σ_{yIII} (MPa)	σ_{yIV} (MPa)	σ_{yV} (MPa)
15	871±21 / 936±23	868	630	528	529	454
25	858±14 / 924±15	874	641	520	521	436
40	853±16 / 919±18	870	644	519	518	428
60	862±10 / 927±18	878	647	516	518	426

Table 7. Experimental yield ($\sigma_{y0.2}$) and ultimate tensile strengths (σ_{UTS}). Yield strength values calculated through the different approaches $\sigma_{y I-V}$ corresponding to the HAZ microstructures at the tested cooling times in the UNS S32304 DSS. The $\sigma_{y0.2}$ and σ_{UTS} values of the as-receive samples were 661 MPa and 718 MPa respectively.

$\Delta t_{12/8}$, s	$\sigma_{y0.2} \pm \delta\sigma_{y0.2}$ / $\sigma_{UTS} \pm \delta\sigma_{UTS}$ (exp.)(MPa)	σ_{yI} (MPa)	σ_{yII} (MPa)	σ_{yIII} (MPa)	σ_{yIV} (MPa)	σ_{yV} (MPa)
15	665±10 / 715±13	908	596	517	517	465
25	649±14 / 696±15	901	600	512	512	456
40	628±17 / 657±17	917	613	517	517	452
60	619±8 / 658±9	914	617	518	518	447

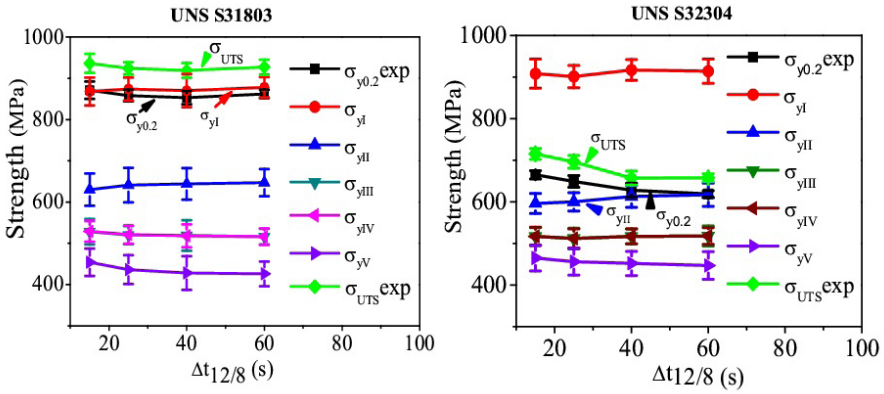

Figure 9. The experimental ultimate tensile strength (σ_{UTS}) and yield strength ($\sigma_{y0.2}$) values, and the calculated yield strength according to the different empirical approaches, $\sigma_{y I-V}$, at the HAZs for the tested cooling times in the UNS S31803 and UNS S32304 DSSs.

This can be due to a reduction of the nitrogen supersaturation in the matrix and a reduction of the favorable nucleation sites. The austenite fraction is more significant at the HAZ microstructures of the UNS S31803 DSS, Figure 3. This is due to a smaller ferrite grain size and higher nitrogen content in the UNS S31803 DSS[13,17]. The GBA volume fraction predominates in the HAZ microstructures of both DSSs for all cooling times, Tables 2 and 4, but this predominance is greater at the HAZ microstructures in the UNS S31803 DSS by the already above exposed. The WA and IGA fractions grow with the cooling time, as does the GBA fraction, but the latter seems to stop growing during the longer cooling times[19]. The IGA and WA are formed at low temperatures with different kinetic mechanisms concerning the formation mechanism of the GBA. The WA laths formed at low temperatures become unstable and break down in small pieces of diamond-shaped austenite for a better partition of the alloy elements[39]. These small diamond-shaped austenite pieces were also considered IGA precipitates in the micrographs. The slight change in the average size of the IGA precipitates and the average width of the WA laths is related to the migration of the partially coherent interphase boundaries of these austenite morphologies[40], where structural dislocations in their broad faces can be appreciated (Figure 4ab) for the tested cooling times.

5.2. Hardness behavior

As the formation mechanisms of the WA laths and IGA precipitates are different from the nucleation and growth mechanisms of the GBA and presumably different nitrogen contents, the Widmanstätten and intragranular austenite particles are harder than the GBA in both DSSs, Figure 5. The hardness values of ferrite at the HAZ microstructures in both DSSs are similar and do not show significant deviations with the tested cooling times. This is corresponded with a previous work where few coalesced nitrides were observed by TEM[19] in some larger ferrite grains at the lower cooling time in the simulated HAZ microstructures of the UNS S31803 DSS. According to this, and the low nitrogen content in both DSS, the hardening contribution by nitride precipitation at these HAZ microstructures must not significantly influence the ferrite hardness. Also, the different austenite morphological forms are harder than the ferrite matrix. This is because almost all the nitrogen partitions to austenite during these cooling times.

Given that the austenite volume fractions are smaller at the HAZ microstructures of the UNS S32304 DSS (see Figure 3), their morphologies have more nitrogen in solution. Therefore, they are harder than the same austenite morphological forms corresponding to the HAZ microstructures in the UNS S31803 DSS (Figure 5). Thus, the hardness difference between the austenite morphological forms (hard phase) and ferrite matrix (soft phase) is higher at the HAZs of the UNS S32304 DSS than at the HAZs of the UNS S31803 DSS for the same cooling times. As shown in Figure 6, the normalized hardnesses corresponding to the HAZ microstructures of the UNS S32304 are closer to the ferrite hardness for the tested cooling times. On the contrary, even though the hardness difference between hard and soft phases is lower at the HAZs of the UNS S31803 DSS, their normalized hardnesses move away from the ferrite hardness. Therefore, the effect of the austenite volume fractions with different morphologies influences the HAZ hardening more than the local hardness values of their constituents in these two DSSs, where nitride precipitation is scarce.

5.3. Analysis of the strengthening mechanisms

To search the influence of the main microstructural parameters (Tables 3 and 5) on the strengthening mechanisms at these HAZs, it is necessary to analyze the tensile test results. As shown in Figure 7, the ratios $\sigma_{UTS}/\sigma_{y0.2}$ are between 1.07 and 1.04 for all the HAZs in both DSSs. These strain-hardening potential (ratios between σ_{UTS} and $\sigma_{y0.2}$) values are too low compared with 1.23 value[41]. Therefore, a good correlation must have between strength and hardness. Thus, the approximation of one-third of hardness equal to yield strength[42] is suitable for determining the local phases' yield strength in these heterogeneous microstructures (HAZ) of both DSSs.

Materials with high σ_{UTS}/σ_{y} ratios could not be fully hardened under the hardness test. The indentations in such materials usually exhibit "sink-in" morphologies after the hardness test, and the hardness is a work-hardened state of the material[21]. On the contrary, in materials with ratios $\sigma_{UTS}/\sigma_{y} \cong 1$, the hardness can represent the intrinsic property of the material when the selected load for the hardness test makes indentations with "pile-up" morphology[21].

The experimental engineering stress-strain curves of these simulated HAZs of both duplex steels showed similar shapes, and their $\sigma_{UTS}/\sigma_{y0.2}$ ratios were approximately equal. However, it is significant that the yield strength ($\sigma_{y0.2}$) values are smaller at the HAZs of the UNS S32304 DSS than the corresponding $\sigma_{y0.2}$ values in the HAZs of the UNS S31803 DSS, Figure 8. This is despite that the hardness values of the constituents at the UNS S32304 HAZs are higher than in the UNS S31803 HAZs.

It is well established that homogeneous structures with small grain size, the grain boundary resistance predominates on the lattice friction during strain[43]. However, in these heterogeneous microstructures (HAZ), as shown in Figure 8, a different situation occurs. The HAZ microstructures with a smaller ferrite grain size (UNS S31803) are less sensitive to the grain boundary resistance during strain. Hence, the mechanical properties ($\sigma_{y0.2}$ and σ_{UTS}) of the HAZs corresponding to the UNS S31803 do not suffer significant changes despite the growth of the ferrite grain size with increasing the cooling time ($\Delta t_{12/8}$). On the contrary, at the HAZs of the UNS S32304 DSS, the yield ($\sigma_{y0.2}$) and ultimate tensile strengths are more sensitive to the ferrite grain size growth during strain.

The previous experimental results can be explained by the predominance of the different austenite morphologies at the HAZ microstructures of the UNS S31803. It is known that for the tested cooling times, the different austenite morphological forms manifest some coherence with ferrite at these HAZs. This is given by the predominance of the γ/δ interfaces with specific orientation relationships (ORs)[19,44]. Figure 4ab shows representative IGA precipitates corresponding to the HAZs with the shorter cooling time in both DSSs. The broad faces in these austenite particles show structural dislocations periodically spaced that accommodate the misfit between the γ/δ lattices. These misfit dislocations arranged periodically in the broad faces reveal specific ORs between the γ/δ lattices[45,46]. Thus, such austenite precipitates having some coherence with ferrite (essentially WA and IGA) introduce friction stress on the dislocations, which raises the level of the stress-strain curve (high yield strength) without markedly altering the dislocation interactions leading to work-hardening[47]. This agrees with the similar values of the $\sigma_{UTS}/\sigma_{y0.2}$ ratios for all the simulated HAZs in both duplex steels.

Furthermore, during the sample deformation, the ferrite should be deformed first. The δ phase has higher stacking fault energy (SFE)[3,48-50] and lower hardness than the different austenite morphologies. Moreover, if many austenite particles have random ORs with ferrite, strain gradients will appear during the sample deformation. The geometrically necessary dislocations located in the ferrite phase near the δ/γ interfaces with random ORs could increase the work-hardening at these HAZs, increasing the $\sigma_{UTS}/\sigma_{y0.2}$ ratio. This shows that the IGA and WA particles with random ORs are not abundant in these HAZs at the tested cooling times.

The above behavior shows the significant effect of the austenite volume fractions with different morphologies and specific ORs on the strengthening mechanisms of the HAZs in these DSSs. Also, as the ferrite grains at the HAZ microstructures in the UNS S31803 DSS are smaller at the tested cooling times, the IGA and the WA volume fractions within the ferrite grains are relatively high, reducing the sensitivity of the yield and ultimate tensile strengths with the ferrite grain size[51].

With the purpose to shed light on the strengthening mechanisms at the HAZs of these DSSs during strain, the experimental yield strengths are compared with the calculated yield strength approaches ($\sigma_{yI\text{-}V}$). These yield strength approaches were calculated, taking into account the corresponding microstructural parameters of each HAZ. The agreement between the computed strengthening approaches with the experimental yield strengths allows seeing the predominance of a particular strengthening mechanism.

As can be appreciated in Figure 9 and Tables 6 and 7 , the best agreement between the experimental yield strength ($\sigma_{y0.2}$) and the calculated yield strength approaches ($\sigma_{yI\text{-}V}$) for the HAZs of the UNS S31803 DSS is given by the approach σ_{yI}. On the other hand, the calculated values according to the approach σ_{yII} seem to correspond well

with the experimental yield strength ($\sigma_{y0.2}$) in the HAZs of the UNS S32304 DSS for these cooling times. This suggests that the mechanical properties of the HAZ ($\sigma_{y0.2}$-σ_{UTS}) are less sensitive with the ferrite grain size when the volume fractions of the austenite morphologies with specific ORs increase, as can be appreciated at the HAZs of the UNS S31803 DSS (more γ/δ interfaces within the δ grain). In this case, the yield strength can be estimated by the σ_{yI} relationship. Thus, the intragranular flow stress of all phases (γ and δ) predominates above the strength contribution due to the additional resistance to dislocation motion caused by the non-coherent δ/GBA boundaries in these HAZs during the strain.

On the other hand, when the volume fractions and dispersion of the different austenite morphologies (IGA and WA) decrease within the ferrite grains, the non-coherent δ/GBA boundary effect significantly influences the HAZ strengthening during the strain. Therefore, the mechanical properties of such HAZs ($\sigma_{y0.2}$-σ_{UTS}) must be more sensitive to the ferrite grain size. By this, the yield strength of these HAZs could be estimated by a Hall-Petch-type relationship. In this case, the contribution due to the additional resistance to dislocation motion caused by the non-coherent δ/GBA grain boundaries during the strain significantly influences the intragranular flow stress of all phases at the HAZs.

The results show that the calculated yield strength approaches ($\sigma_{yI\text{-}V}$) allow assessing the influence of the local phase features on the strengthening mechanisms that govern the stress-strain behavior in the HAZs of both DSSs. Thus, the yield strength ($\sigma_{y0.2}$) of the HAZs corresponding to the UNS S31803 DSS can be estimated through the hardness values according to a σ_{yI} relationship. In these HAZs the local phase features are characterized by ferrite grain sizes between 100-200 μm and high volumetric fractions of the different austenite morphologies with specific ORs. Nevertheless, for the same cooling times, the yield strength ($\sigma_{y0.2}$) of the HAZs in the UNS S32304 DSS can be estimated by a σ_{yII} relationship. It is given by the greater ferrite grain sizes (> 200 μm) and lower austenite volume fractions with specific ORs within the ferrite grain. Finally, different heat inputs on the HAZ strengthening are more significant in the UNS S32304 because yield and tensile strength are more sensitive to the ferrite grain size.

6. Conclusions

This research was focused in the influence of the local phase features on the strengthening mechanisms that govern the stress-strain behavior of simulated HAZs corresponding to two commercial DSSs. According to a detailed microstructural analysis of the simulated HAZs and the empirical approaches developed in this research, the following conclusion can be high-lighted:

1. The volumetric fraction of the different austenite morphologies with specific ORs within the ferrite grain at the HAZs of these DSSs determine the predominance of the intragranular flow stress or the non-coherent δ/GBA grain boundaries effects during the strain.
2. The HAZ cooling rate determines the predominance of specific or random ORs between the austenite precipitates (IGA and WA) and ferrite in the microstructures. When specific ORs predominate, the increment of the work-hardening at these HAZs is small.
3. The WA and IGA volume fractions (hard phase) determine much more at the HAZ strength than the hardness difference between hard and soft phases at the tested cooling times in these DSSs.
4. The yield strength ($\sigma_{y0.2}$) at the HAZs in the UNS S31803 DSS, considering their microstructural parameters and chemical composition, could be more represented by a σ_{yI} relationship where the intragranular flow stress predominates. The yield strength strength ($\sigma_{y0.2}$) at the HAZs in the UNS S32304 DSS could be defined by a σ_{yII} relationship where the grain boundary effects during strain have a significant influence.

7. Acknowledgments

The authors wish to thank Fundação de Amparo à Pesquisa do Estado do Rio de Janeiro (FAPERJ) andCoordenação de Aperfeiçoamento de Pessoal de Nivel Superior (CAPES) in Brazil for the financial support offered by the project 09/2014 - PVE - CAPES.One of the authors (EVM) also thanks FAPERJ for financial support (Processo No E-26/201-535/218) and CAPES for the project PVE 88881.064968/2014-01). L. Olaya would like to thank CAPES for the scholarship to conduct part of his doctoral research as a Visiting Student at the Ohio State University. Processo: PDSE - 88881.133489/2016-01 and Programa CAPES: PROSUP/Bolsas, Processo 1363910. One of the authors (E. V. Morales) thanks the anonymous reviewer for his review which significantly improved the article.

8. References

1. Horvath W, Taberning B, Werner E, Uggowitzer P. Microstructures and yield strength of nitrogen alloyed superduplex steels. Acta Mater. 1997;45(4):1645-54.
2. Johansson J, Oden M, Zeng XH. Evolution of the residual stress state in a duplex stainless steel during loading. Acta Mater. 1999;47(9):2669-84.
3. Tao P, Gong JM, Wang YF, Jiang Y, Li Y, Cen WW. Characterization on stress-strain behavior of ferrite and austenite in a 2205 duplex stainless steel based on nanoindentation and finite element method. Results in Physics. 2018;11:377-84.
4. Gadelrab KR, Li G, Chiesa M, Souier T. Local characterization of austenite and ferrite phases in duplex stainless steel using MFM and nanoindentation. J Mater Res. 2012;27(12):1573-9.
5. Baltazar Hernandez V, Panda SK, Kuntz ML, Zhou Y. Nanoindentation and microstructure analysis of resistance spot welded dual phase steel. Mater Lett. 2010;64(2):207-10.
6. Hirota N, Yin F, Azuma T, Inove T. Yield stress of duplex stainless steel specimens estimated using a compound Hall-Petch equation. Sci Technol Adv Mater. 2010;(11):025004.
7. Li X, Miodownik AP, Saunders N. Modelling of materials properties in duplex stainless steels. Mater Sci Technol. 2002;18:861-8.
8. Li X, Miodownik AP, Saunders N. Simultaneous calculation of mechanical properties and phase equilibria. J Phase Equilibria. 2001;22(3):247-53.
9. Fan Z, Tsakiropoulos P, Mindownik AP. A generalized law of mixtures. J Mater Sci. 1994;29:141-50.
10. Jang M-H, Moon J, Lee T-H, Park SJ, Han HN. Effect of nitrogen partitioning on yield strength in nitrogen-alloyed

duplex stainless steel during annealing. Metall Mater Trans, A Phys Metall Mater Sci. 2014;45A:1653-8.
11. Foct J, Akdut N. Cleavage-like fracture at austenite in duplex stainless steel. Scr Metall Mater. 1993;29:153-8.
12. Moverare JJ, Odén M. Influence of elastic and plastic anisotropy on the flow behavior in a duplex stainless steel. Metall Mater Trans, A Phys Metall Mater Sci. 2002;33A:57-71.
13. Hertzman S, Ferreira PJ, Brolund B. An experimental and theoretical study of the heat-affected zone austenite reformation in three duplex stainless steels. Metall Mater Trans, A Phys Metall Mater Sci. 1997;28:277-85.
14. Sun Q, Wang J, Li HB, Li Y, Hu YD, Bai JG, et al. Chi phase after short-term aging and corrosion behavior in 2205 duplex stainless steel. J Iron Steel Res Int. 2016;23:1071-9.
15. Pohl M, Storz O, Glogowsky T. Effect of intermetallic precipitations on the properties of duplex stainless steel. Mater Charact. 2007;58:65-71.
16. Kokawa H, Tsory E, North TH. Nitride precipitation in duplex stainless steel weld metal. ISIJ Int. 1995;35:1277-83.
17. Hertzman S, Charles J. On effect of nitrogen on duplex stainless steels. Rev Metall. 2011;108:413-25.
18. Liao J. Nitride precipitation in weld HAZ of duplex stainless steel. ISIJ Int. 2001;41:460-7.
19. Morales EV, Pozo JA, Olaya L, Kassab E, Ponciano JAC, Ghavami K, Bott IS. Remarks on the evolution and performance of the different austenite morphologies at the simulated HAZs of a 2205 duplex stainless steel. Jour Mater Res Technol. 2019;8(5):3936-49.
20. Yang Y, Yang B, Li J, Wang J. The effect of large heat input on the microstructure and corrosion behavior of simulated heat affected zone in 2205 duplex stainless steel. Corros Sci. 2011;531:3756-63.
21. Zhang P, Li SX, Z. Zhang ZF. General relationship between strength and hardness. Mater Sci Eng A. 2011;529:62-73.
22. Johansson J, Odén M. Load sharing between austenite and ferrite in duplex stainless steels during cycle loading. Met Mat Trans. 2000;31A(6):1557-70.
23. Tamura I, Tomota Y, Ozawa H. Strength and ductility of iron-nickel-carbon alloys composed of austenite and martensite with various strength. In: Proceeding of the 3rd International Conference on Strength of Metals and Alloys. London: Institute of Metals and Iron and Steel Institution; 1973. p. 611-15.
24. An XH, Wu SD, Zhang ZF, Figueiredo RB, Gao N, Langdon TG. Evolution of microstructural homogeneity in copper processed by high-pressure torsion. Scr Mater. 2010;63:560-3.
25. Li H, Ebrahimi F. Grain size dependence of tensile behavior in monocrystalline Ni-Fe alloys. Mater Sci Eng A. 2003;347:93-101.
26. Lu L, Schwaiger R, Shan ZW, Dao M, Lu K, Suresh S. Nano-sized twins induce high rate sensitivity of flow stress in pure copper. Acta Mater. 2005;53:2169-79.
27. Sanders PG, Youngdahl CJ, Weertman JR. The strength of nanocrystalline metals with and without flaws. Mater Sci Eng A. 1997;234-236:77-82.
28. Anthamatten BR, Cui M, Uggowitzer P. In ergebnisse der werkstoff-forschung. Züric: Verlag der Schweizerischen Akademie der Werkstoffwissenschaften; 1987. p. 205-18.
29. Kubasehewski O. Iron-binary phase diagrams. Berlin. Springer-Verlag; 1982: p. 67-70.
30. Armstrong RW, Codd I, Douthwaite RN, Petch NJ. The plastic deformation of polycrystalline aggregate. Philos Mag. 1962;7:45-8.
31. Fischmeiter H, Karlsson B. Plasticity of two-phase materials with a coarse microstructure. Z Metallk. 1997;68(5):311-27.
32. Uggowitzer P, Stuwe HP. Plasticity of ferritic-martensitic 2-phase steels. Z Metallk. 1982;73:277-85.
33. Nam WJ, Bae CM, Lee CS. Effect of carbon content on the Hall-Petch parameter in cold drawn pearlitic steel wires. J Mater Sci. 2002;37(11):2243-9.
34. Sieurin H, Zander J, Sandström R. Modelling solid solution hardening in stainless steels. Mater Sci Eng A. 2006;415:66-71.
35. Sieurin H, Sandström R. Austenite reformation in the heat-affected zone of duplex stainless steel 2205. Mater Sci Eng A. 2006;418:250-6.
36. Muthupandi V, Srinivasan PB, Seshadri SK, Sundaresan S. Effect of weld metal chemistry and heat input on the structure and properties of duplex stainless steel welds. Mater Sci Eng A. 2003;358:9-16.
37. Liou HY, Hsieh RI, Tsai WT. Microstructure and pitting corrosion in simulated heat-affected zones of duplex stainless steels. Mater Chem Phys. 2002;74:33-42.
38. Wang SH, Chiu PK, Yang JR, Fang J. Gamma (γ) phase transformation in pulsed GTAW weld metal of duplex stainless steel. Mater Sci Eng A. 2006;420:26-33.
39. Wu TH, Wang JJ, Li HB, Jiang ZH, Liu CM, Zhang HY. Effect of heat input on austenite microstructural evolution of simulated heat affected zone in 2205 duplex stainless steel. J Iron Steel Res Int. 2018;26:435-41.
40. Aaronson HI, Enomoto M, Lee JK. Mechanisms of diffusional phase transformations in metals and alloys. Boca Raton: CRC Press; 2010.
41. Pavlina EJ, Van Tyne CJ. Correlation of yield strength and tensile strength with hardness for steels. JMEPEG. 2008;17:888-93.
42. Tabor D. The hardness of solids. Rev Phys Techn. 1970;1(145):147-52.
43. Kashyap BP, Tangri K. On the Hall-Petch relationship in type 316L stainless steel at room temperature. Scr Metall Mater. 1990;24:1777-82.
44. -Haghdadi N, Cizek P, Hodgson PH, Tari V, Rohrer GS, Beladi H. Effect of ferrite-to-austenite phase transformation path on the interface crystallographic character distribution in a duplex stainless steel. Acta Mater. 2018;145:196-209.
45. Van der Merwe JH. On the stresses and energies associated with inter-crystalline boundaries. Proc Phys Soc A. 1950;63:616-37.
46. Howell PR, Southwick PD, Honeycombe RWK. The austenite/ferrite interface in a duplex alloy steel: structure and associated diffraction effects. J Microsc. 1979;116(1):151-8.
47. Kelly A, Nicholson RB. Precipitation hardening. Prog Mater Sci. 1963;10:151-391.
48. Reick W, Pohl M, Padilha AF. Determination of stacking fault energy of austenite in a duplex stainless steel. Steel Res. 1996;67(6):253-6.
49. Wasilewski RJ. B.C.C. Stacking fault energies. Scr Metall. 1967;1(1):45-7.
50. Zhang X, Wang P, Dianzhong L, Li Y. Multi-scale study on the heterogeneous deformation behavior in duplex stainless steel. J Mater Sci Technol. 2021;72:180-8.
51. Jiang M, Devincre B, Monnet G. Effects of the grain size and shape on the flow stress: a dislocation dynamics study. Int J Plast. 2019;113:111-24.